arXiv:1602.00885v3 [hep-ph] 18 Feb 2016

ASYMPTOTIC REGIMES FOR HADRON DIFFRACTIVE SCATTERINGS AND COULOMB INTERACTION. ARGUMENTS FOR THE BLACK DISK MODE

V.V. ANISOVICH, V.A. NIKONOV

National Research Centre "Kurchatov Institute", Petersburg Nuclear Physics Institute, Gatchina 188300, Russia

J. NYIRI

Institute for Particle and Nuclear Physics, Wigner RCP, Budapest 1121, Hungary

Received Day Month Year
Revised Day Month Year

Comparative analysis of the interplay of hadron and Coulomb interactions in $pp^{\pm}$ scattering amplitudes is performed in a broad energy interval, $\sqrt{s} = 1 - 10^6$ TeV, for two extreme cases: for the asymptotic interactions of hadrons in black disk and resonant disk modes. The interactions are discussed in terms of the K-matrix function technique. In the asymptotic regime the real part of the hadronic amplitude is concentrated in both cases on the boundary of the disks in the impact parameter space but the LHC energy region is not asymptotic for the resonant disk mode that lead to a specific interplay of hadronic and coulombic amplitudes. For the pp scattering at $\sqrt{s} \sim 10$ TeV an interplay of the hadron and Coulomb interactions in the resonant disk modes is realized in a shoulder in $d\sigma_{el}/d\mathbf{q}^2$ at $\mathbf{q}^2 \sim 0.0025 - 0.0075$ GeV^2. The absence of such a shoulder in the data at 8 TeV can be considered as an argument against the resonant disk mode.

PACS numbers: 13.85.Lg, 13.85.-t, 13.75.Cs, 14.20.Dh

1. Introduction

New data[1] for $d\sigma_{el}/d|t|$ at $\sqrt{s} = 8$ TeV in the region $|t| = 0.0006 - 0.2061$ GeV^2 shed light on the problem of the asymptotic regime of hadron cross sections at ultrahigh energies.

The analysis of the pre-LHC[2–6] and LHC[7–10] data for hadronic total cross sections and diffractive scattering cross sections points to a steady growth of the optical density in the impact parameter space, $T(b, \ln s)$, with increasing energy, $\sqrt{s}$. At LHC energy the profile function of the pp-scattering amplitude reaches the black disk limit at small b. Two extreme scenarios are possible at larger energies, $\sqrt{s} \gtrsim 100$ TeV.

First, the profile function gets frozen in the black disk limit, $T(b) \simeq 1$, while the radius of the black disk, $R_{black\ disk}$, is increasing with $\sqrt{s}$ providing $\sigma_{tot} \sim \ln^2 s$, $\sigma_{el} \sim \ln^2 s$, $\sigma_{inel} \sim \ln^2 s$. The black disk regime was studied in a number of papers, see refs.[11–14] and references therein.

In another scenario the profile function continues to grow at $\sqrt{s} \gtrsim 100$ TeV approaching the maximal value, $T(b) \simeq 2$, that means the resonant disk mode. In this mode the disk radius, $R_{resonant\ disk}$, increases providing the $\ln^2 s$-growth of the total and elastic cross sections, $\sigma_{tot} \sim \ln^2 s$, $\sigma_{el} \sim \ln^2 s$, but a slower increase of inelastic cross section, $\sigma_{inel} \sim \ln s$, see refs.[15–17] .

Hadron physics at ultrahigh energies is a physics of large energy logarithms, $\ln s \equiv \xi >> 1$[18–20] , and increasing parton disks[21–25] . The black disk picture corresponds to the non-coherent parton interactions in hadron collisions. In the resonant disk mode the partons interact coherently thus providing a maximal cross section corresponding to the Froissart limit[26] .

In this paper, considering an interplay of hadron and Coulomb interactions, we concentrate our attention on the resonant disk mode; the corresponding consideration of the interplay in the black disk mode was performed in refs.[27–29] .

The asymptotic regime in the resonant disk mode starts at essentially larger energies than in the black disk regime. In the LHC energy region the resonant disk profile function increases more rapidly than that in the black disk mode. It results in a larger real part of the scattering amplitude and, correspondingly, in a larger interference of hadronic and coulombic terms. At $\sqrt{s} \sim 10$ TeV the interplay of hadronic and coulombic interactions reveals itself in a shoulder in $d\sigma_{el}/d\mathbf{q}^2$ at $\mathbf{q}^2 \sim 0.0025 - 0.0075$ GeV^2. The shoulder is not seen in the data for pp scattering at 8 TeV[1] that provides an argument in favour of the black disk mode.

In Section 2 we calculate the real part of the hadronic amplitude in the resonant mode. Inclusion of the Coulomb interaction is performed in Section 3, a comparative analysis of results in the black disk and resonant disk modes is presented. In these section we demonstrate the data at 8 TeV[1] versus calculations of $d\sigma_{el}/d|t|$ in the black disk and resonant disk modes - the comparison definitely argues in favour of the black disk mode.

2. Hadronic amplitude and K-matrix function

For the hadronic scattering amplitude with switched off Coulomb interaction we write:

$$A^H(\mathbf{q}^2,\xi) = \int d^2b e^{i\mathbf{qb}} T^H(b,\xi),$$

$$T^H(b,\xi) = 1 - \eta(b,\xi)\exp\left(2i\delta(b,\xi)\right) = \frac{-2iK^H(b,\xi)}{1 - iK^H(b,\xi)}\ , \qquad (1)$$

where $\xi = \ln s$ and $b = |\mathbf{b}|$. The complex function $K^H(b,\xi)$ presents part of amplitude without elastic rescatterings (or, with inelastic processes in the intermediate states only).

For the imaginary and real parts of the introduced functions we write[27,28] :

$$-iK^H(b,\xi) = K^H_{\Im}(b,\xi) - iK^H_{\Re}(b,\xi) \simeq K^H_{\Im}(b,\xi) - i\frac{\pi}{2}\frac{\partial K^H_{\Im}(b,\xi)}{\partial\xi}\ . \qquad (2)$$

At the asymptotic regime the imaginary part of the amplitude is a generating function for the real part of the amplitude, the asymptotic equality $[\sigma_{tot}(pp)/\sigma_{tot}(p\bar{p})]_{\sqrt{s}\to\infty} = 1$ is supposed for that, see refs.[27,28] for details. The total and diffractive cross sections read:

$$\sigma_{tot} = 2\int d^2b T^H_{\Im}(b,\xi), \qquad 4\pi\frac{d\sigma_{el}}{d\mathbf{q}^2} = (1+\rho^2)\Big|A^H_{\Im}(\mathbf{q}^2)\Big|^2, \tag{3}$$

with the usual notation $A^H_{\Re}(\mathbf{q}^2,\xi)/A^H_{\Im}(\mathbf{q}^2,\xi) = \rho(\mathbf{q}^2,\xi)$. Taking into account that ρ^2 is small ($\rho^2 \sim 0.01$ and asymptotically $\rho \sim 1/\ln s$) one can approximate:

$$\Big|A^H_{\Im}(\mathbf{q}^2,\xi)\Big| \simeq 2\pi^{\frac{1}{2}}\sqrt{\frac{d\sigma_{el}}{d\mathbf{q}^2}}, \tag{4}$$

Eq. (4) makes possible direct calculations of the real part of the scattering amplitude, $A^H_{\Re}(\mathbf{q}^2,\xi)$, on the basis of the energy dependence of the diffractive scattering cross section. The corresponding calculations were performed in ref.[28] using preLHC[2–6] and LHC[7–10] data. The results were extrapolated in the region $\sqrt{s} = 10 - 10^6$ TeV using the black disk mode hypothesis for the asymptotic regime. The next step, an inclusion of the Coulomb interaction into consideration of the scattering amplitude, was made in refs.[27,29] .

2.1. *Resonant disk and K-matrix function*

From the data it follows that both $T^H(b)$ and $-iK^H(b)$ are increasing with energy, being less than unity. If the eikonal mechanism does not quench the growth, both characteristics cross the black disk limit getting $T^H(b) > 1$, $-iK^H(b) > 1$. If $-iK^H(b) \to \infty$ at $\ln s \to \infty$, which corresponds to a growth caused by the supercritical pomeron ($\Delta > 0$), the diffractive scattering process gets to the resonant disk mode.

For following the resonant disk switch-on we use the two-pomeron model with parameters providing the description of data at 1.8 TeV and 7 TeV[17,30] , namely:

$$\begin{aligned} K^H_{\Im}(b) &= \int \frac{d^2q}{(2\pi)^2}\exp\Big(-i\mathbf{qb}\Big)\sum g^2 s^{\Delta} e^{-(a+\alpha\xi)\mathbf{q}^2)} \\ &= \sum \frac{g^2}{4\pi(a+\alpha'\xi)}\exp\Big[\Delta\xi - \frac{\mathbf{b}^2}{4(a+\alpha'\xi)}\Big], \qquad \xi = \ln\frac{s}{s_0}. \end{aligned} \tag{5}$$

The real part of the K-matrix function is determined in accord with Eq. (2).

The following parameters are used for the leading and the next-to-leading pomerons:

parameters	leading pole	next-to-leading
Δ	0.20	0
α'_P [GeV^{-2}]	0.18	0.14
a [GeV^{-2}]	6.67	2.22
g^2 [mb]	1.65	27.2
s_0 [GeV^2]	1	1

(6)

The description of the data at 1.8 TeV and 7 TeV within the resonant disk mode and neglecting the real part of the amplitude was performed in ref.[17] . The inclusion of the real part into consideration of these data leads to some corrections of the parameters, see[30] . We use here parameters of ref.[30] for the presentation of diffractive scatterings at 8 TeV and 14 TeV.

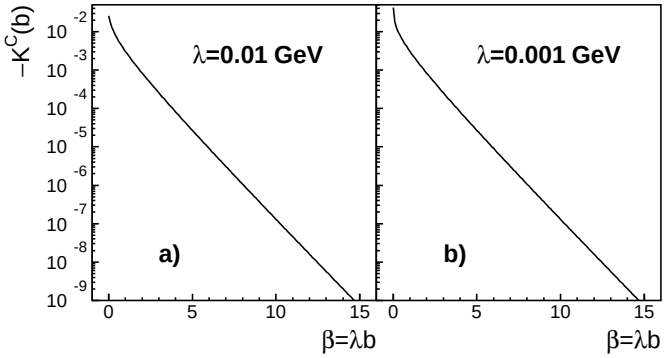

Fig. 1. The K-matrix function, $-K^C(b)$, for the pure Coulomb interaction in pp collision at different λ, we use $\beta = \lambda b$ for abscissa with a) $\lambda = 0.01$ GeV and b) $\lambda = 0.001$ GeV.

3. Diffractive scattering amplitude at ultrahigh energy and Coulomb interaction

The interplay of hadronic and Coulomb interactions was studied in a set of papers, see[31–37] and references therein. In the region of ultrahigh energies and small $\mathbf{q}^2$, the K-matrix function technique allows to take into account directly the combined action of hadronic and Coulomb interactions $(H + C)$.

3.1. *Interplay of hadronic and Coulomb interactions in the K-matrix function technique*

We consider two types of scattering amplitudes and corresponding profile functions: the amplitude with combined interaction taken into account, $A^{C+H}(\mathbf{q}^2, \xi)$ and $T^{C+H}(b, \xi)$, and that with the switched-off Coulomb interaction, $A^H(\mathbf{q}^2, \xi)$ and $T^H(b, \xi)$.

For the combined interaction profile function we write:

$$T^{C+H}(b,\xi) = \frac{-2iK^{C+H}(b,\xi)}{1 - iK^{C+H}(b,\xi)} = \frac{-2i\left(K^C(b) + K^H(b,\xi)\right)}{1 - i\left(K^C(b) + K^H(b,\xi)\right)}\,, \tag{7}$$

where the Coulomb interaction is written as:

$$A^C(\mathbf{q}^2) = \pm i f_1(\mathbf{q}^2)\frac{4\pi\alpha}{\mathbf{q}^2 + \lambda^2} f_2(\mathbf{q}^2),$$

$$-2iK^C(b) = \pm i \int \frac{d^2q}{(2\pi)^2} e^{i\mathbf{qb}} f_1(\mathbf{q}^2)\frac{4\pi\alpha}{\mathbf{q}^2 + \lambda^2} f_2(\mathbf{q}^2)\,. \tag{8}$$

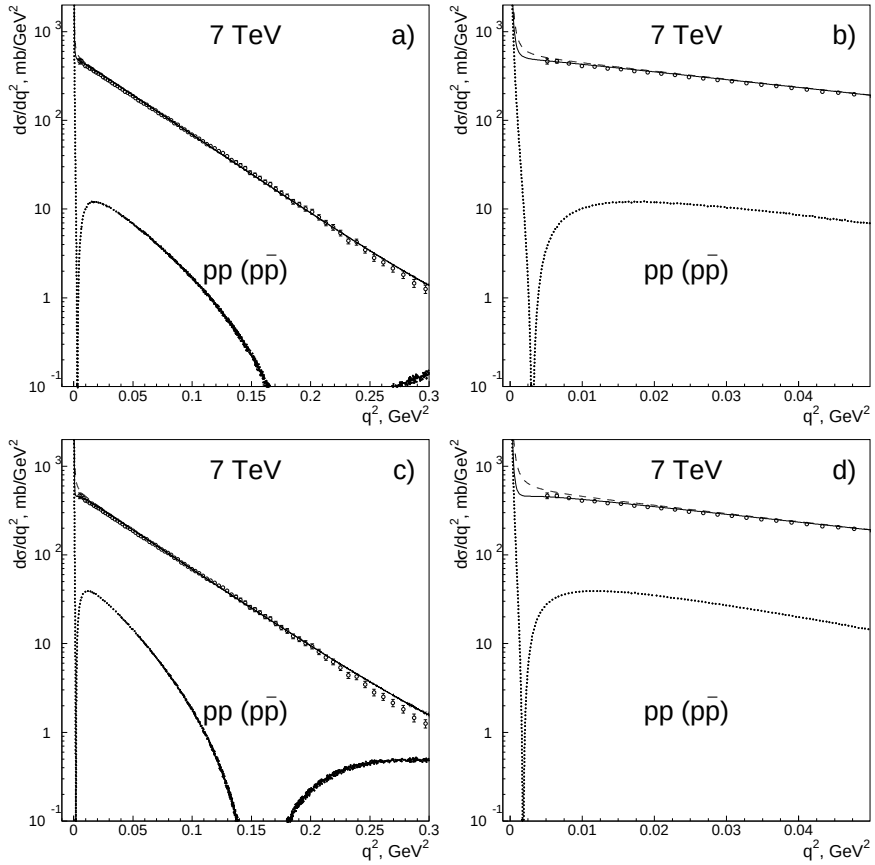

Fig. 2. Diffractive scattering cross section for pp at 7 TeV (TOTEM[7]) versus description with interplay of hadronic and Coulomb interactions (Eq. (10), λ=0.001 GeV): figures (a,b) refer to the black disk mode, figures (c,d) refer to the resonant disk case; solid curves refer to pp, dashed ones to $p\bar{p}$. Dotted curves show a contribution of the real part in the pp scattering, the last term in Eq. (10).

Here $\alpha = 1/137$; the upper/lower signs refer to the same/opposite charges of the colliding particles. The cutting parameter λ, which removes the infrared divergency, can tend to zero in the final result for $A^{C+H}(\mathbf{q}^2, \xi)$. Colliding hadron form factors, $f_1(\mathbf{q}^2)$ and $f_2(\mathbf{q}^2)$, guarantee the convergence of the integrals at $\mathbf{q}^2 \to \infty$; for the $pp^{\pm}$ collisions we use:

$$f_1(\mathbf{q}^2) = f_2(\mathbf{q}^2) = \frac{1}{(1 + \frac{\mathbf{q}^2}{0.71 GeV^2})^2}\,. \tag{9}$$

In Fig. 1 we show $-K^C(b)$ for $\lambda = 0.01$ GeV (Fig. 1a) and 0.001 GeV (Fig. 1b). At large b the $K^C(b)$ is a scaling function in terms of $\beta = \lambda b$, the β-scaling gets broken at small β.

For a diffractive scattering cross section with Coulomb interaction taken into

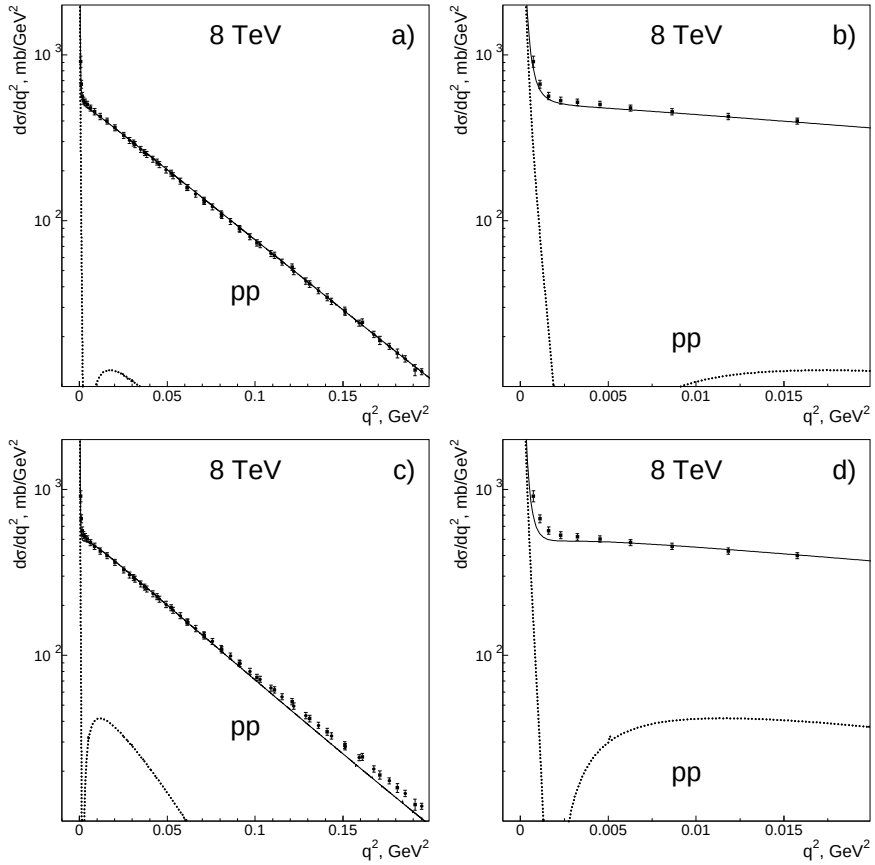

Fig. 3. Diffractive scattering cross section for pp at 8 TeV (TOTEM[1]) versus description with interplay of hadronic and Coulomb interactions (Eq. (10), λ=0.001 GeV): figures (a,b) refer to the black disk mode, figures (c,d) refer to the resonant disk case; solid curves refer to pp. Dotted curves show a contribution of the real part in the pp scattering, the last term in Eq. (10).

account we write now:

$$A^{H+C}(\mathbf{q}^2,\xi) = \int d^2b e^{i\mathbf{qb}} T^{H+C}(b,\xi),$$
$$4\pi\frac{d\sigma_{el}}{d\mathbf{q}^2} = \left|A^{H+C}_{\Im}(\mathbf{q}^2)\right|^2 + \left|A^{H+C}_{\Re}(\mathbf{q}^2)\right|^2. \quad (10)$$

The diffractive scattering cross sections with Coulomb interaction taken into account are shown in Figs. 2, 3, 4 for $\sqrt{s}$ =7, 8, 14 TeV.

3.2. *Interference of hadronic and Coulomb interactions*

At the LHC energies ($\sqrt{s} \sim 10$ TeV) the real part of the resonant disk amplitude demonstrates an essentially stronger contribution compared to that in the black

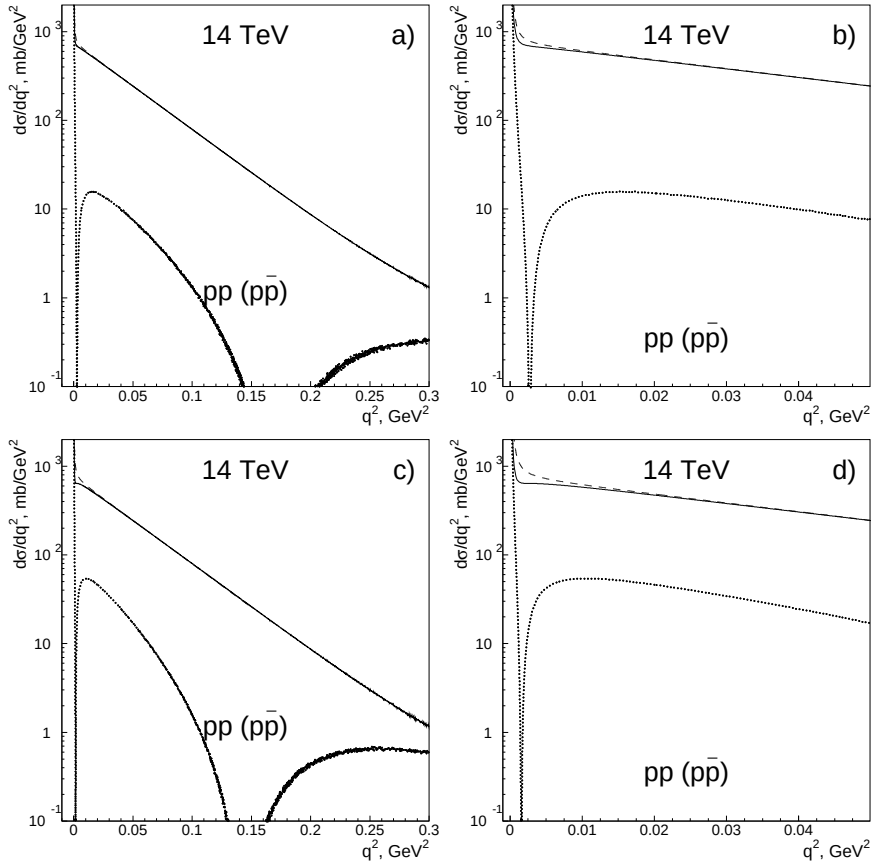

Fig. 4. Diffractive scattering cross sections for $pp^{\pm}$ at 14 TeV (Eq. (10), λ=0.001 GeV): The figures (a,b) refer to the black disk mode and (c,d) to the resonant disk one; solid curves refer to pp, dashed ones to $p\bar{p}$. Dotted curves show a contribution of the real part in the pp scattering, the last term in Eq. (10).

disk mode, see Figs. 2, 3, 4 for $\left|A^{H+C}_{\Re}(\mathbf{q}^2)\right|^2$ and Figs. 5, 6 for $K^{H+C}(b,\xi)$ and $T^{H+C}(b,\xi)$. For the resonant disk mode it results in a shoulder in the pp diffractive cross section $\frac{d\sigma_{el}(\mathbf{q}^2)}{d\mathbf{q}^2}$ at $\mathbf{q}^2 \sim 0.0025 - 0.0075$ GeV^2. The shoulder is a qualitative attribute of the resonant disk picture in the pp scattering, and it means that a presence of the shoulder, or its absence, can serve as a sign for the disk modes.

3.3. *Asymptotic regimes in the black disk and resonant disk modes*

For the black disk mode the valuable asymptotic regime works at $\sqrt{s} \gtrsim 10^2$ TeV. The real parts of $K^{H+C}(b,\xi)$ and $T^{H+C}(b,\xi)$ (see Figs. 5d, 6d) have peak shapes, with fixed maximal peak values $\sim$0.12 and $\sim$0.10, respectively. At large b where the pure Coulomb interaction works ($b > R_{disk\,radius}$) the K-matrix function (and the

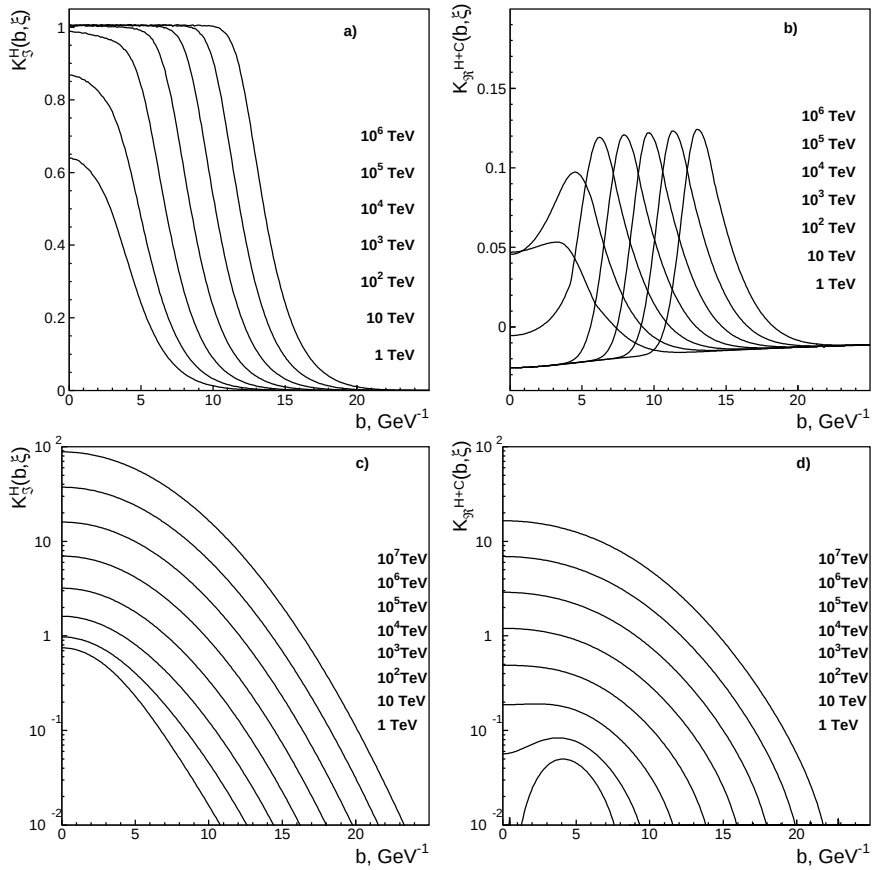

Fig. 5. K-matrix functions for *pp* scattering (imaginary and real parts) in the energy region $\sqrt{s} = 1 - 10^6$ TeV; figures (a,b) refer to the black disk mode, (c,d) to the resonant disk mode.

profile function) is negative for the *pp* scattering as it should be for particles with the same electric charge.

In the resonant disk mode the asymptotic value of the imaginary part of the amplitue reaches its maximal value, $T^{H+C}_{\Im}(b,\xi) \simeq 2$ at $\sqrt{s} \gtrsim 10^5$ TeV only. The maximal values of the real part continue to increase at $\sqrt{s} \gtrsim 10^6$ TeV. The stable maximal values are reached at $\sqrt{s} \gtrsim 10^{19}$ TeV where $T^{H+C}_{\Re}(maximal) \simeq 0.6$. Negative values of the real part of the *pp* scattering profile function, $T^{H+C}_{\Re}(b,\xi) < 0$ at $b > R_{disk\,radius}$, are inherent to resonant disk mode as well.

3.4. *The 8 TeV data as an argument for the black disk mode*

The resonant disk picture at $\sqrt{s} \sim 10$ TeV results in an essentially larger value of the real part in the scattering amplitude than that in the black disk mode. The large real part is realized in a shoulder in the *pp* diffractive cross section at $\mathbf{q}^2 \sim 0.0025 - 0.0075$ GeV^2. The shoulder is absent in the data at 8 TeV[1] that agree

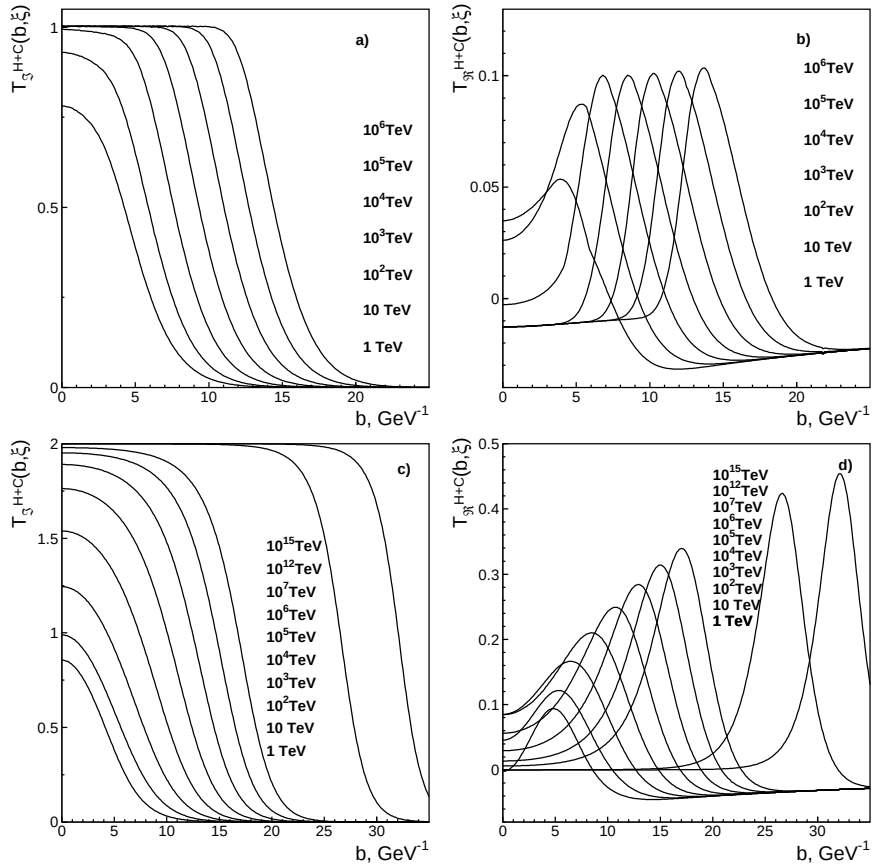

Fig. 6. Profile functions for *pp* scattering (imaginary and real parts) in the energy region $\sqrt{s} = 1 - 10^6$ TeV with the Coulomb interaction taken into account; (a,b) refer to the black disk mode, (c,d) to the resonant disk mode.

with calculations for the black disk picture.

Figures 7 demonstrate the region of small momenta transferred for the *pp* diffractive cross sections at 7 TeV (the data from ref.[7]) and 14 TeV, the solid curves refer to the resonant disk mode and the dashed curve to the black disk one. The data[7] do not distinguish the modes being well described in both of them.

Figures 8 show the 8 TeV data[1] at small $\mathbf{q}^2$. The data are described in terms of the black disk mode while the resonant disk gives essentially smaller values of $\frac{d\sigma}{d\mathbf{q}^2}$ at ~ 0.0010 GeV^2.

The data for $\rho(\mathbf{q}^2 = 0, \xi) = A_{\Re}^H(0,\xi)/A_{\Im}^H(0,\xi)$ prefer also the black disk mode:

$\sqrt{s}$	7 TeV	8 TeV	14 TeV
ρ(data)		0.12 ± 0.03[1]	
ρ(black disk)	0.17	0.17	0.16
ρ(resonant disk)	0.34	0.34	0.33

. (11)

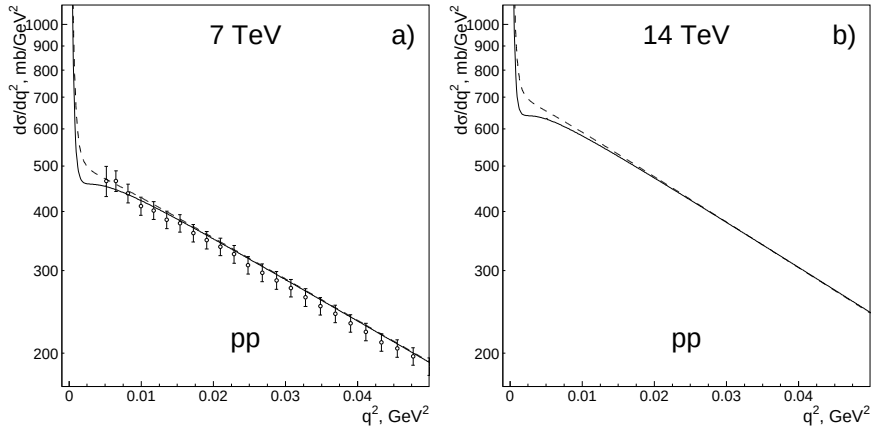

Fig. 7. Diffractive scattering cross sections for pp at 7 TeV (a) (Eq. (10), λ=0.001 GeV). The dashed line refers to the black disk mode and the solid one to the resonant disk mode.

So, the 8 TeV data[1] provides convincing arguents in favour of the black disk picture at ultrahigh energies.

The extraction of the real part of the amplitude is based on the asymptotical relation (2), the question arises how small deviations from (2) effect the interplay of the hadron and Coulomb interactions. In Fig. 8b we show the diffractive scattering cross section with the real part enlarged by a factor 1.10 that demonstrates the sensitivity of $\frac{d\sigma}{d\mathbf{q}^2}$ to the value of $\rho(\mathbf{q}^2,\xi)$. It also tells that the procedure of the Eq. (2) determines the real part of the amplitude within $\sim$10% accuracy.

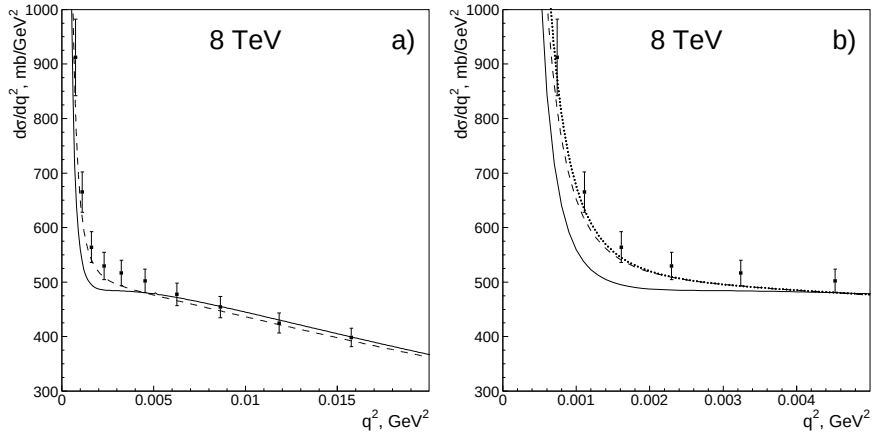

Fig. 8. Diffractive scattering cross sections for pp at 8 TeV (Eq. (10), λ=0.001 GeV). The dashed line refers to the black disk mode and the solid one to the resonant disk mode. The dotted line (fig. b) shows the diffractive cross section with real part enlarged in factor 1.10.

4. Conclusion

Our studies are performed in terms of the K-matrix function, in hadron physics the K-matrix techniqe was used for non-relativistic processes[38] and relativistic ones[39–41] as well as for high energy hadron-hadron collisions[42] . For ultrahigh energy production processes the technique was applied in refs.[43,44] .

The problem of parton cloud structure of hadrons with ultrahigh energy is a subject of lively discussions[45–50] . A slow growth of the parton cloud radius with energy increase argues for a glueball origin of the parton clouds[23–25] , the glueball origin of the parton clouds leads to the universality of all hadron total cross sections[51] .

Performing the unitarization of the scattering amplitude we restrict ourselves to the consideration of the comparatively small momenta transferred region thus concentrating our attention on peripheral interaction of the conventional pomerons. At large $\mathbf{q}^2$ other types of the input pomerons are possible as well as non-pomeron short-range contributions (for example, see[52–55]) but these problems are beyond the present studies.

We study the asymptotic regime supposing for the parton clouds two different extreme modes: the black disk mode and resonant disk one. In the black disk mode the diffractive scattering occurs due to non-coherent parton interactions while the resonant disk scattering is the result of coherent interaction of partons with the same impact parameter b; the resonant disk mode realizes the maximal growth of the amplitude compatible with the Froissart constraint[26] .

In a number of papers[13,16,23] the appearance of a black spot at LHC energy in the profile function at small b is emphasized but the pre-LHC and 7 TeV LHC data do not supply us with information to determine definitely the asymptotic mode of the scattering amplitude. The 8 Tev data[1] fill a gap in the information noticeably.

The Coulomb and hadronic interaction interplay is realized due to the interference in the real part of the amplitude, and the real part of the resonant disk amplitude is essentially larger than that for the black disk mode. In the pp scattering the large interference results in the resonant disk mode as a shoulder in the region $\mathbf{q}^2 \sim 0.0025 - 0.0075$ GeV^2. The shoulder is not observed in 8 TeV data[1] this is an argument in favour of the realization of the black disk picture at ultrahigh energies.

Acknowledgement

We thank Y.I. Azimov and A.V. Sarantsev for useful discussions. The work was supported by RSGSS-4801.2012.2 grant.

References

1. G. Atchev et al. [TOTEM Collaboration], CERN-PH-EP-2015-325.
2. G. Arnison *et al.* [UA1 Collaboration], Phys. Lett. B **128**, 336 (1983).
3. M. Bozzo *et al.* [UA4 Collaboration], Phys. Lett. B **147**, 385 (1984).

4. N. A. Amos *et al.* [E-710 Collaboration], Phys. Lett. B **247**, 127 (1990).
5. C. Augier *et al.* [UA4/2 Collaboration], Phys. Lett. B **316**, 448 (1993).
6. F. Abe *et al.* [CDF Collaboration], Phys. Rev. D **50**, 5518 (1994).
7. G. Latino [on behalf of TOTEM Collaboration], EPJ Web Conf. **49**, 02005 (2013).
8. G. Aad *et al.* [ATLAS Collaboration], Eur. Phys. J. C **72**, 1926 (2012).
9. V. Khachatryan *et al.* [CMS Collaboration], Phys. Rev. D **92**, 012003 (2015).
10. B. Abelev *et al.* [ALICE Collaboration], Eur. Phys. J. C **73**, 2456 (2013).
11. M.L. Good and W.D. Walker, Phys. Rev. **120**, 1857 (1960).
12. L. G. Dakhno and V. A. Nikonov, Eur. Phys. J. A **5**, 209 (1999).
13. M.M. Block and F. Halzen, Phys. Rev. **D86**, 0501504 (2013).
14. V.V. Anisovich, V.A. Nikonov and J. Nyiri, Phys. Rev. D **88**, 094015 (2013).
15. S.M. Troshin and N.E. Tyurin, Int. J. Mod. Phys. A **29**, 1450151 (2014).
16. I.M. Dremin, Bull. Lebedev Phys. Inst. **42**, 21 (2015) [Kratk. Soobshch. Fiz. **42**, 8 (2015)] [arXiv:1404.4142 [hep-ph]].
17. V.V. Anisovich, V.A. Nikonov and J. Nyiri, Phys. Rev. D **90**, 074005 (2014).
18. T.K. Gaisser and T. Stanev, Phys. Lett. B **219**, 375 (1989).
19. M.M. Block, F. Halzen and B. Margolis, Phys. Lett. B **252**, 481 (1990).
20. R.S. Fletcher, Phys. Rev. D **46**, 187 (1992).
21. V.V. Anisovich, V.M. Shekhter, Sov. J. Nucl. Phys. **28**, 561 (1978); [Yad. Fiz. **28**, 1079 (1978)].
22. V.V. Anisovich, E.M. Levin, M.G. Ryskin, Sov.J.Nucl.Phys. **29**, 674 (1979); [Yad.Fiz. **29**, 1311 (1979)].
23. V.V. Anisovich, K.V. Nikonov and V.A. Nikonov, Phys. Rev. D **88**, 014039 (2013).
24. V.V. Anisovich, V. A. Nikonov and J. Nyiri, Int. J. Mod. Phys. A **29**, 1450096 (2014).
25. V.V. Anisovich, Phys. Usp. **58**, 963 (2015); [UFN **185**, 1043 (2015)].
26. M. Froissart, Phys. Rev. **123**, 1053 (1961).
27. V.V. Anisovich, V. A. Nikonov and J. Nyiri, arXiv:1508.02140 [hep-ph].
28. V.V. Anisovich, V.A. Nikonov and J. Nyiri, Int. J. Mod. Phys. A **30**, 1550188 (2015).
29. V. V. Anisovich and V. A. Nikonov, arXiv:1601.07015 [hep-ph] (to be published in Mod. Phys. Lett. A).
30. V. V. Anisovich, V. A. Nikonov and J. Nyiri, arXiv:1602.00885 [hep-ph].
31. H.A. Bethe, Annals Phys. **3**, 190 (1958).
32. L.D. Soloviev, Zh. Exp. Theor. Fiz. **49**, 292 (1966) [Sov. Phys. JETP **22**, 205 (1966)].
33. G.B. West and D. R. Yennie, Phys. Rev. **172**, 1413 (1968).
34. V. Franco, Phys. Rev. D **7**, 215 (1973).
35. R. Cahn, Z. Phys. C **15**, 253 (1982).
36. V. Kundrat and M. Lokajicek, Z. Phys. C **63**, 619 (1994).
37. J. Kaspar, V. Kundrat, M. Lokajicek and J. Prochazka, Nucl. Phys. B **843**, 84 (2011).
38. V.V. Anisovich and A.A. Anselm, Physics-Uspekhi, **88**, 117 (1966);[UFN **88**,287 (1966)].
39. I.J.R. Aitchison, Nucl. Phys. A189, 417 (1972).
40. I.J.R. Aitchison, arXiv:1507.02697[hep-ph] (2015).
41. V.V. Anisovich and A.V. Sarantsev, Eur. Phys. J. **A 16**, 229 (2003).
42. A.V. Anisovich and V.V. Anisovich Phys. Lett. **B275**, 491 (1992).
43. V.V. Anisovich, M.A. Matveev, V.A. Nikonov Int. J. Mod. Phys. **A29** 1450176 (2014).
44. V.V. Anisovich, M.A. Matveev, V.A. Nikonov Int. J. Mod. Phys. **A30** 1550054 (2015).
45. E. Martynov, arXiv:1412.0269[hep-ph].
46. F. Nemes, T. Csörgő and M. Csanád, Int. J. Mod. Phys. A **30** 1550076 (2015).
47. M. Giordano and E. Megiolaro, Phys. Lett. B **744**, 263 (2015).
48. I.M. Dremin, Adv. High Energy Phys. 2015, 912743 (2015).

49. I.M. Dremin, Phys. Usp. **58**, 61 (2015); [UFN **185**, 65 (2015)].
50. S.M. Troshin and N.E. Tyurin, arXiv:1601/00483 [hep-ph].
51. V.N. Gribov, Sov. J. Nucl. Phys. **17**, 313 (1973).
52. A.V. Kotikov and L.N. Lipatov, Nucl. Phys. **B661**, 19 (2003).
53. K. Kang and H. Nastase, Phys. Lett. **B624**, 125 (2005).
54. E. Gotsman, E.M. Levin and U. Maor, arXiv:1203.2419 (2012).
55. A.K. Likhoded, A.V. Luchinsky and A.A. Novoselov, Phys. Rev. D**82**, 114006 (2010).